Advanced Functional Materials

ADVANCED FUNCTIONAL MATERIALS
www.afm-journal.de

RESEARCH ARTICLE

Flexoelectricity-Driven Self-Powered Photodetectors for Information Transmission and Image Processing

Zhaotan Gao[1] | Hongli Chen[1] | Can Zhao[1] | Zhangchen Hou[1] | Zian Hong[1] | Ruiqi Jiang[1] | Yawei Li[1] | Liyan Shang[1] | Liangqing Zhu[1] | Jinzhong Zhang[1,2] | Jian Zhang[1] | Zhigao Hu[1,3]

[1]Technical Center for Multifunctional Magneto-Optical Spectroscopy (Shanghai), Engineering Research Center of Nanophotonics & Advanced Instrument (Ministry of Education), Department of Physics, School of Physics, East China Normal University, Shanghai, China | [2]School of Communication and Electronic Engineering, East China Normal University, Shanghai, China | [3]Collaborative Innovation Center of Extreme Optics, Shanxi University, Taiyuan, Shanxi, China

Correspondence: Jinzhong Zhang (jzzhang@ee.ecnu.edu.cn) | Jian Zhang (52264700035@stu.ecnu.edu.cn) | Zhigao Hu (zghu@ee.ecnu.edu.cn)

Received: 9 November 2025 | **Revised:** 13 March 2026 | **Accepted:** 26 March 2026

Keywords: 2D semiconductor | flexoelectric effect | image enhancement and recognition | optical communication | self-powered photodetection

ABSTRACT

In the digital information age, self-powered photodetectors are crucial for meeting the demands of high-density integration and low power consumption. The flexoelectric effect provides a mechanical approach for the development of high-efficiency and low-energy consumption photoelectronic devices. Here, an asymmetric suspended structure model is proposed by taking advantage of the inherent mechanical flexibility of 2D materials. The asymmetric transverse flexoelectric polarization field formed internally enables WSe_2 to have excellent self-powered photodetection capabilities in the visible to near-infrared range. The device demonstrates excellent photoelectric performance ($R \sim 6\times10^3$ A W^{-1}) and ultra-weak light detection capability ($P_{in} = 1.5\,\mu$W cm^{-2}). Moreover, the coupling mechanism between photoelectric and flexoelectric effects has been elucidated through kelvin probe force microscopy (KPFM) and first-principles calculations. In particular, the device achieved stable information transmission and image processing under weak light conditions. The visual gain has been enhanced by more than two orders of magnitude. This research result highlights the potential applications of the flexoelectric effect and lays a solid foundation for the design and integrated development of high-performance photoelectronic devices.

1 | Introduction

In recent years, the continuous development of the information age has led to an explosive growth in the total amount of data, which imposes higher requirements for information transmission and detection [1]. Compared with traditional communication systems, optical communication systems have been widely studied due to their advantages of large data capacity, ultra-fast transmission speeds, and high levels of efficiency and reliability [2, 3]. As a core component in modern optical communication systems, information storage, and biomedical imaging, the performance of photodetectors directly determines the transmission quality and efficiency of the entire system [3–7]. Therefore, the development of photodetectors with high responsivity, high detectivity, and low power consumption has gradually become a research focus [8, 9]. With the deep integration of artificial intelligence and internet of things technologies, the traditional detection of optical signals is no longer sufficient to meet the information processing demands in complex scenarios [10]. Photodetection technology has been extended to the field of intelligent perception on the basis of stable optical signal transmission [11]. Building an integrated photoelectric intelligent system with image perception, storage, and processing capabilities has become an effective way to achieve more efficient and low power image recognition [12].

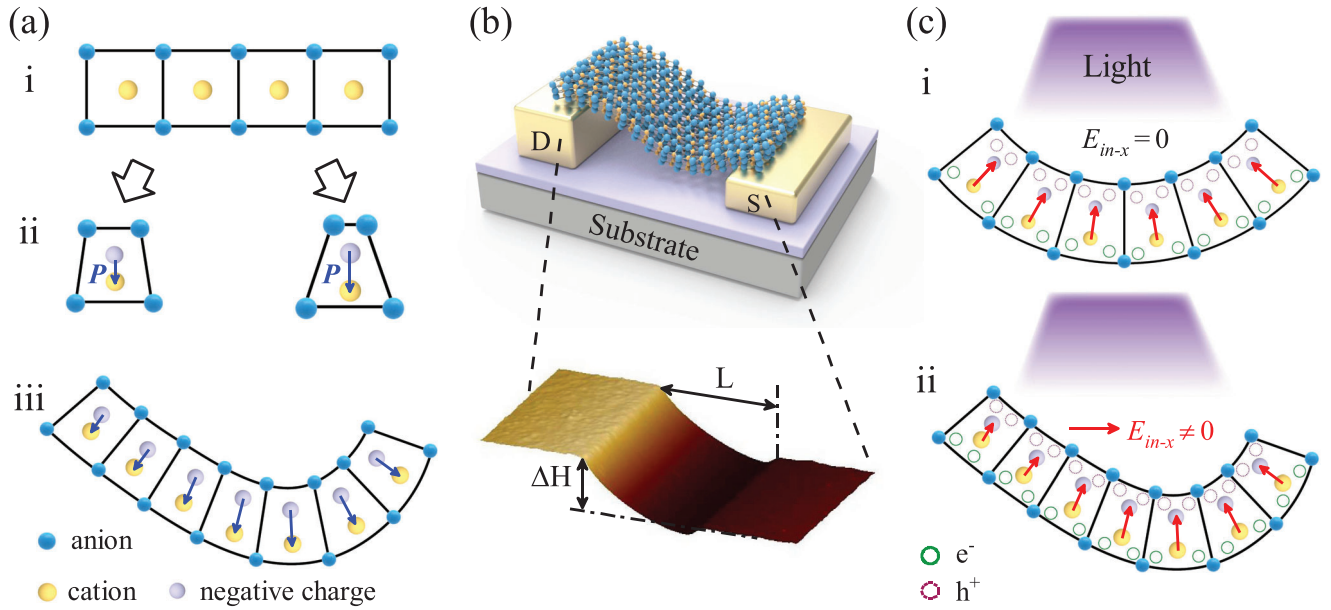

FIGURE 1 | Asymmetric suspended structure model with flexoelectric and photoelectric coupling effects. (a) Asymmetric flexoelectric response via strain engineering in centrosymmetric microarchitectures. (b) A 3D-schematic device with an asymmetric suspended structure and the corresponding AFM topographic image. (c) Flexoelectric and photoelectric coupling effects in (i) symmetric and (ii) asymmetric suspended structure.

Compared with other materials, 2D van der Waals (vdW) materials are widely used in photoelectronic device research due to high absorption coefficient, tunable bandgap, and excellent mechanical flexibility [13, 14]. Wang et al. constructed a photodetector based on the $MoTe_2/WS_2/MoTe_2$ heterostructure, effectively modulated the Fermi level alignment, and achieved a specific detectivity of 1.82×10^{14} Jones [15]. Recently, Zeng et al. developed a strain-based application strategy for 2D materials using ZnO/WSe_2/graphene vdW heterostructures, which enhanced the external quantum efficiency (*EQE*) from 11.4% to 35.3% [16]. However, traditional photodetectors typically require an external power supply to maintain normal operation, which increases the complexity and power consumption of the system and limits the device applicability. Self-powered photodetectors can use the energy generated by illumination to provide the required power for operation. This design significantly reduces the need for external power supplies and improves the energy efficiency and autonomy of the system [17]. Recently, researchers have conducted extensive work on material optimization, structural design, and performance enhancement of self-powered photodetectors [5, 17, 18]. Detectors based on the piezophototronic effect continuously explore new material systems and device structures to achieve better photoelectric detection performance and self-powered capabilities [19, 20]. Although self-powered photodetectors have shown great potential in the field of optical communication, further improving the photodetection performance under weak illumination remains a challenge. Therefore, it is essential to explore novel self-powered devices to achieve superior photoelectronic performance.

Recently, mechanical strain has demonstrated unique advantages in the modification of 2D materials [21, 22], especially in band structure modulation and interface optimization, enabling devices to exhibit excellent electromechanical responses [23–27]. Tang et al. achieved significantly enhanced photoresponse in MoS_2 based on strain tuning [28]. Strain is becoming a reliable means to improve the performance of optoelectronic devices [28–31]. As a voltage-free method, the flexoelectric effect can regulate the material through the coupling between the strain gradient and the electric field and the light field [32, 33]. Compared with the traditional piezoelectric effect, the strain gradient mechanism relied on by the flexoelectric effect is widely applicable [34, 35]. Since mechanical bending is inversely proportional to the scale, the flexoelectric effect dominates in low-dimensional materials. Meanwhile, 2D materials with excellent mechanical flexibility provide ideal conditions for achieving large strain gradients [36, 37]. It enables the properties of 2D materials to be effectively regulated, such as carrier concentration, photoresponse, and ferroelectric polarization [36, 38, 39]. However, the improvement of the flexoelectric effect in photoresponse has not been as expected, especially in passive devices. One possible explanation is that the strain gradient used to generate the flexoelectric polarization field is usually limited to a single or fixed direction. For example, the net flexoelectric polarization only shows a resultant field in the vertical direction due to the influence of symmetrical structures [38, 40, 41]. Therefore, it is necessary to improve the flexoelectric polarization field control method at the present stage.

In this work, we propose a method for achieving flexoelectric effects to regulate 2D materials in both the longitudinal and transverse directions by asymmetric suspended structures. At the nanoscale, the coupling between transverse flexoelectric polarization and light field endows 2D materials with exceptional self-powered capabilities. The experimental results show that the asymmetric suspended structure model enables the WSe_2-based photodetector to exhibit outstanding photoelectric performance ($R \sim 6{\times}10^3$ A W^{-1}), ultra-weak light detection capability ($P_{in} = 1.5$ μW cm^{-2}) and excellent device stability. The wide applicability of the structural model is demonstrated by

the results from WSe_2 and InSe photodetectors. Stable information transmission and image processing under weak light have been achieved based on the asymmetric suspended structure. Compared with conventional photodetectors, the visual gain has been enhanced by more than two orders of magnitude. This work achieves high performance of passive devices at the device scale, and deeply understands the coupling mechanism between flexoelectric and photoelectric effects. This provides a new design strategy for the development of low-power and high-performance devices and expands the practical application of the flexoelectric effect.

2 | Results and Discussion

2.1 | Asymmetric Suspended Structural Model

Figure 1a illustrates the theoretical model of asymmetric flexoelectric polarization in 2D semiconductors under nonuniform strain conditions. The centers of positive and negative charges coincide within a centrosymmetric structure, as shown in Figure 1ai. It means the unit cell has a net dipole moment of zero. In Figure 1aii, the separation of the positive and negative charge centers induces a flexoelectric polarization field along the strain gradient when a unit cell is subjected to nonuniform strain. The magnitude of flexoelectric polarization field is positively correlated with the strain gradient. Note that the flexoelectric polarization field of varying magnitudes and directions can be generated within the same material by introducing different strain gradients. The superposition of the flexoelectric polarization field forms a non-zero net flexoelectric polarization field in vector space, as shown in Figure 1aiii. The flexoelectric polarization field provides the necessary conditions for the self-powered photodetection.

Figure 1b shows an asymmetric suspended structure with 2D van der Waals materials, which forms asymmetric bending under the influence of external forces due to the exceptional mechanical flexibility. 2D van der Waals materials exhibit high carrier mobility and demonstrate strong photoelectric coupling capabilities [42, 43]. The flexoelectric polarization field is uniformly distributed spatially in symmetric structure models, as shown in Figure 1ci. The photogenerated charges can be rapidly separated and uniformly distributed under the flexoelectric polarization field [24, 25, 44]. The asymmetry of the bending state leads to the asymmetry of the flexoelectric polarization field on the left and right sides of the channel, which causes the suspended film to form a transverse built-in electric field ($E_{in-x} \neq 0$). And the photogenerated charges can form directional movement under the action of the built-in electric field, as shown in Figure 1cii. Therefore, the asymmetric suspended structure can achieve the transverse adjustment of the flexoelectric polarization field, and realize the self-powered photodetection.

2.2 | Self-Powered Effect in Asymmetric Suspended Structure-Based Photodetectors

Figures 2a and Figure S2a show an asymmetric suspended photodetector with WSe_2 as a light absorbing layer and channel. The thick and thin electrodes are defined as drain (D) and source (S) electrodes, respectively. The different electrode height results in a height disparity ($\Delta H \sim 163$ nm) for the WSe_2 channel. The atomic force microscopy (AFM) images and the corresponding line profiles show a bending depth of about 183 nm, which is less than the electrode thickness (~250 nm). It means that the suspended WSe_2 nanosheet does not touch the SiO_2 substrate. In addition, Figure S2b reveals that the WSe_2 nanosheet prepared by mechanical exfoliation has an average thickness of about 9 nm with clean and smooth surface. The Raman spectra exhibit that WSe_2 nanosheets have high crystalline quality (Figure S2c). The photoluminescence (PL) spectrum shows that the bandgap of WSe_2 nanosheets is approximately 1.49 eV (Figure S2d).

In Figure 2b, the photocurrent (Iph) of the asymmetric suspended WSe_2 photodetector increases as the laser power density increases. It indicates that the asymmetric suspended device exhibits an excellent photoresponse. Note that the output characteristic curves do not pass through the origin under illumination. It means the device exhibits photocurrent at $V_{DS} = 0$ V, which is defined as short-circuit current (I_{SC}). The I_{SC} gradually increases as the laser power density increases. It means that the built-in electric field formed in the asymmetric suspended structure can drive the photogenerated charges to move stably. And the voltage (V_{DS} = -0.1 V) is defined as the open-circuit voltage (V_{OC}) when the photocurrent is zero [15]. The existence of I_{SC} and V_{OC} indicates that the device has self-powered photodetection capability at the low laser power density ($P_{in} \leq 26.5\ \mu W\ cm^{-2}$, $\lambda = 405$ nm). Figure 2c shows that photocurrent is stable under various pulsed laser power densities. It means that the asymmetric suspended WSe_2-based photodetectors exhibit excellent photodetection stability under laser pulse. The output characteristic curves and photocurrent curves ($V_{DS} = 0$ V) at different wavelengths ($\lambda = 520$ and 638 nm) confirm that the photodetector achieves outstanding photodetection performance across the visible range (Figure S3). Figure S4 shows that WSe_2 photodetectors based on asymmetric suspended structures exhibit stable photoresponse ($V_{DS} = 0$ V) at 1550 nm ($E_g = 0.8$ eV) due to the regulation of the bandgap ($E_g = 1.49$ eV) of WSe_2 nanosheets by the flexoelectric effect [24], which is confirmed by the infrared PL spectra (Figure S5).

As one of physical quantities to measure the detection performance of photoelectric devices, responsivity (R) is defined by the following formula as: $R = I_{ph}/(PS)$, where $I_{ph} = I_{light}$-I_{dark}, P is laser power density, S is the effective channel area [11]. Without external driving voltage, the responsivity of the asymmetric suspended WSe_2-based photodetector gradually decreases with the laser power density (cf. Figure 2d). The photodetector has a responsivity of up to 6×10^3 A W^{-1} at $V_{DS} = 0$ V, which is better than most reported photodetectors of the same type [45–47]. The asymmetric suspended photodetector has a much lower dark current ($I_{dark} \sim 1.58 \times 10^{-13}$ A) than that of a flat photodetector ($I'_{dark} \sim 1.17 \times 10^{-11}$ A) at $V_{DS} = 0.1$ V (Figures S6 and S7). Especially, the dark current level of the asymmetric suspended WSe_2-based photodetector decreases to 1.68×10^{-14} A at $V_{DS} = 0$ V (Figure S7), which is much lower than those of other similar-type of self-powered photodetectors [5, 48, 49]. The non-photogenerated carrier transport in the WSe_2 layer is significantly suppressed. The current noise power density shows that the asymmetric suspended WSe_2-based photodetector has an excellent detection capability for weak light (Figure S8).

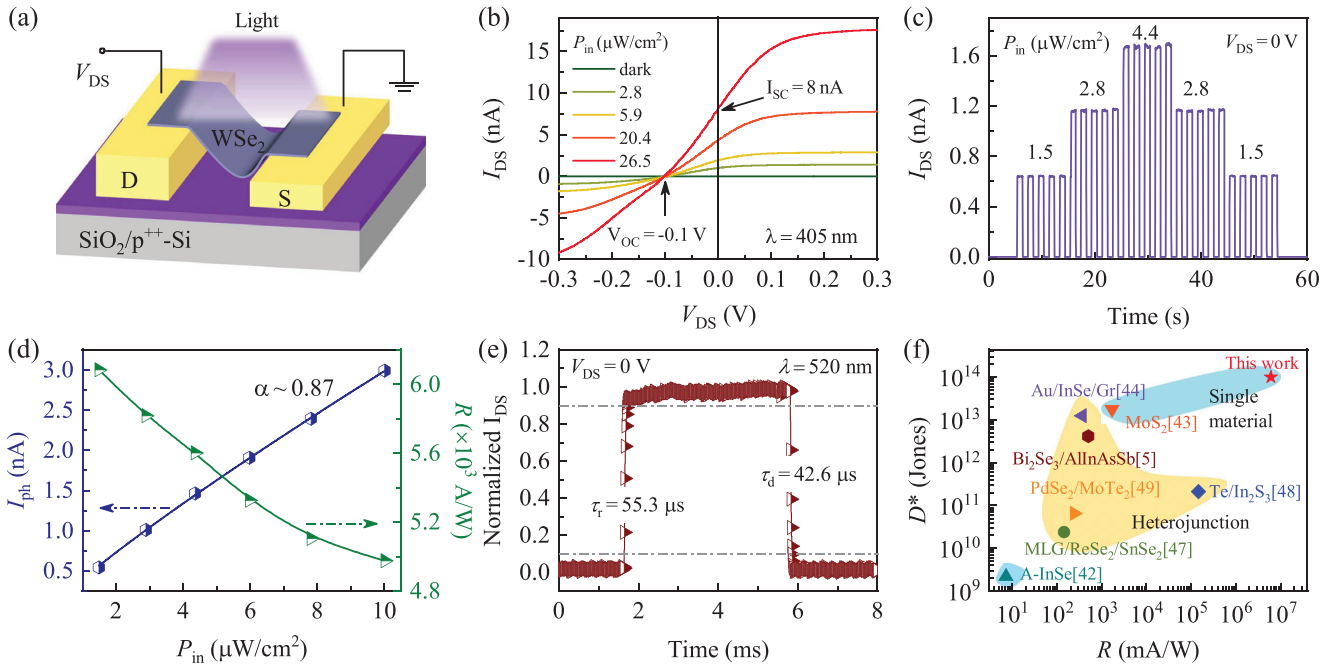

FIGURE 2 | Photoelectric characteristics of an asymmetric suspended WSe_2-based photodetector. (a) A 3D-schematic asymmetric suspended WSe_2-based photodetector under illumination. (b) Output characteristic curves illuminated with various laser power densities from 0 to 26.5 μWcm^{-2} in linear coordinates (λ = 405 nm). (c) Photocurrent at different pulsed laser power densities and V_{DS} = 0 V. (d) Photocurrent and responsivity as a function of laser power density at V_{DS} = 0 V. (e) Normalized photocurrent for evaluating response speeds (τ_r and τ_d). (f) Detectivity comparison of the asymmetric suspended WSe_2-based photodetectors and other self-powered photodetectors based on 2D-layered semiconductors.

Figure S9 shows the variation of *I*SC with laser power density within different laser power ranges. The fitting formula is a power-law formula: $I_{ph} = nP^{\alpha}$, where n is the fitting factor, and α is the power factor. Note that the ideal value of α is 1, while electron-hole recombination and carrier capture cause α to be less than 1 [11]. To reduce the shielding effect of photogenerated charges and ensure that the built-in electric field generated by the flexoelectric effect plays a dominant role [47], the I_{SC} as a function of laser power density within the low-power range was plotted (P_{in} < 10 μW cm^{-2}), as shown in Figure 2d. The fitting results show that α ≈ 0.87. To further explore the contribution of the asymmetric suspended structure model to self-powered photodetection, the symmetric suspended, symmetric non-suspended, and asymmetric non-suspended structures photodetectors were fabricated based on WSe_2 nanosheets, as shown in Figures S10–S12. The output characteristic curves of the four types photodetectors show that no V_{OC} or I_{SC} is generated under various laser power densities. It indicates that the self-powered photodetection capability originates from the asymmetric suspended structure.

Compared with the flat photodetector (α ≈ 0.81 and V_{DS} = -0.1 V, Figure S6), the asymmetric suspended structure reduces the trapping effect at the substrate interface. The main reason for the reduction of the interface capture effect lies in the complete separation of WSe_2 nanosheets from SiO_2/Si (Figure S2a). The suspended structure design can prevent all phonon coupling and pinning effects from the substrate [50]. The photoresponse of flat, symmetrical/asymmetrical suspended/non-suspended structures show that the asymmetric suspended WSe_2-based photodetectors exhibit excellent self-powered photoresponse, which is attributed to the asymmetrical structure breaking the symmetry of the flexoelectric polarization field in the lateral direction in WSe_2 (Table S1). It means that the internal driving force generated by the asymmetric suspended structure can effectively promote the separation and transport of photogenerated carries. The absence of self-powered performance in the symmetrical suspended structure indicates that the influence of piezoelectric effect on the suspended device could be neglected (Figure S10). Therefore, the influence of flexoelectric effect instead of piezoelectric effect is considered for the self-powered performance of the asymmetric suspended device [51].

Fast photoelectric response is a key performance indicator of photodetectors. The response speed at V_{DS} = 0 V was measured under the action of a 520 nm laser. As shown in Figure 2e, the rise time and decay time of the asymmetric suspended WSe_2 photodetector were measured to be 55.3 and 42.6 μs, respectively. In addition, by analyzing the frequency-dependent photoelectric response when the signal attenuates to 70% of its initial value at the modulation frequency within the visible light range, the -3,dB cut-off frequency was measured to be 9.3 kHz (Figure S13). The rise time τ_r estimated by the formula τ_r = 0.35/f(-3 dB) is 37.6 μs, and the slit length is shorter than the measured response time. The specific detectivity is defined as: $D^* = \sqrt{AB}/NEP$, where A is the effective area of the device and B is the bandwidth [52, 53]. And the external quantum efficiency is defined as: $EQE = hcR/(e\lambda)$, where the c, h, λ, and e are the speed of light in vacuum, Planck's constant, the laser wavelength, and the elementary charge [5]. The asymmetric suspended WSe_2-based photodetector achieves a specific detectivity of 5.8×10^{14} Jones, and an *EQE* of 1.86×10^{6}% when the signal equals the noise. Note that the power density of the input laser is P_{in} = 1.5 μW cm^{-2}, whereas conventional photodetector architectures require

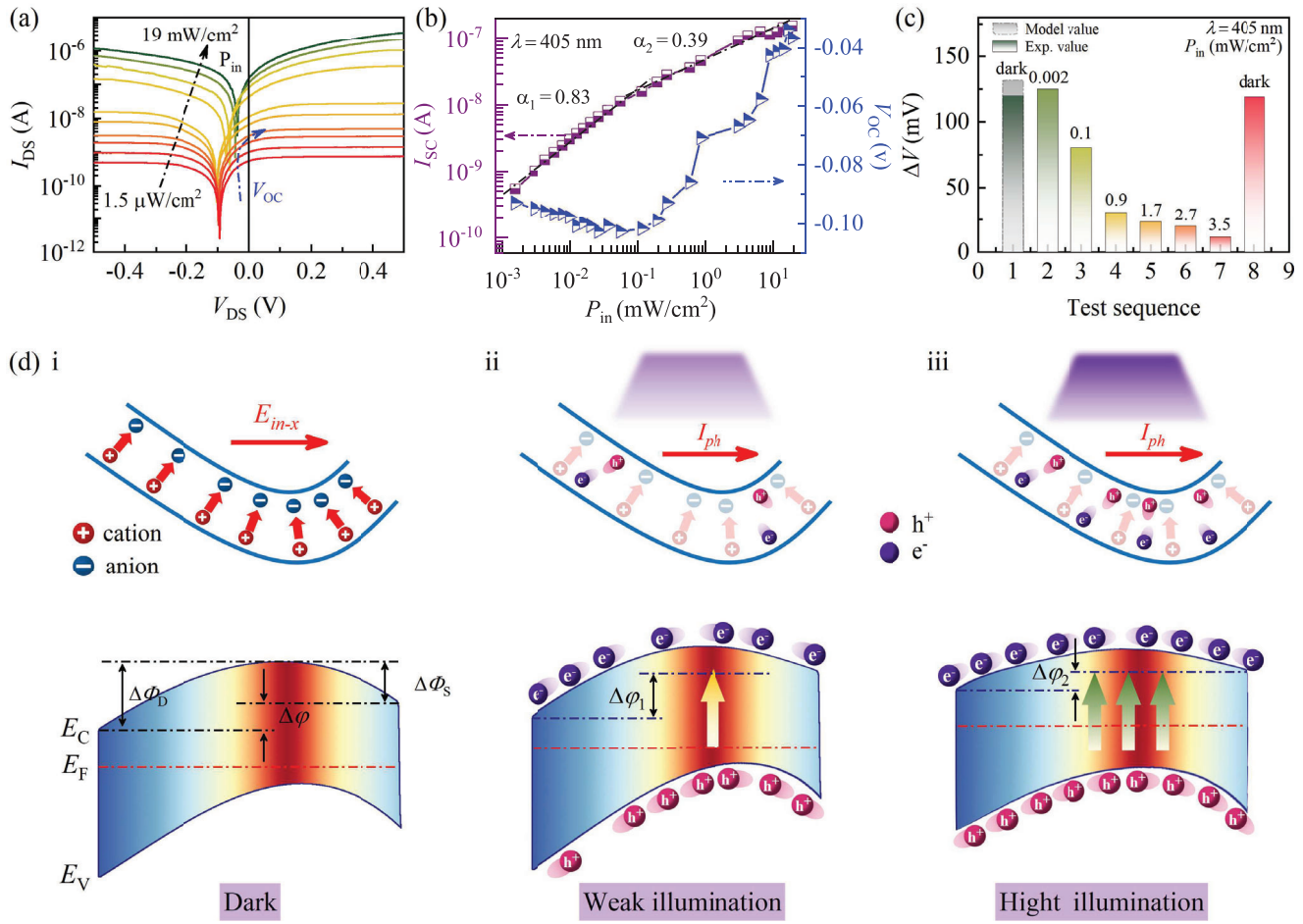

FIGURE 3 | Mechanism diagram of self-powered photodetection in an asymmetric suspended WSe_2-based structure. (a) Output characteristic curves at various laser power densities from 1.5 μW cm^{-2} to 19 mW cm^{-2} on a logarithmic scale. The blue arrow indicates the variation trend of the V_{OC} with the laser power density. (b) The V_{OC} and I_{SC} of asymmetric suspended WSe_2 photodetectors as a function of laser power density in log scale (λ = 405 nm). (c) Surface potential difference at equidistant positions at various P_{in}, and the "model value" represents the built-in electric field value calculated based on the analytical model for the transverse flexoelectric polarization field. (d) Charge distribution and the corresponding band diagram of an asymmetric suspended WSe_2 under (i) Dark ($|\Delta\varphi|$), (ii) weak ($|\Delta\varphi_1| > |\Delta\varphi|$), and (iii) High illumination ($|\Delta\varphi_2| < |\Delta\varphi|$).

optical excitation with power densities exceeding 16 μW cm^{-2} to generate measurable photoresponse. It indicates that the asymmetric suspended WSe_2 photodetector has an excellent weak photodetection capability. Moreover, compared with other self-powered photodetectors based on 2D materials in the visible range, the asymmetric suspended photodetector exhibits superior self-powered photodetection performance (cf. Figure 2f) [5, 54–56]. In addition, InSe-based photodetectors with the asymmetric suspended structure also exhibit excellent self-powered photodetection capability (Figure S14, Supporting information). It indicates that the self-powered photodetection comes from the asymmetric suspended structure and has a wide applicability.

2.3 | Mechanisms of Asymmetric Structure Governed Transverse Flexo-Photoelectric Coupling

To further investigate the generation mechanism of photocurrent, the output characteristics of the asymmetric suspended WSe_2 photodetector were measured within a broader range of laser power densities (1.5 μWcm^{-2}– 19 mW cm^{-2}) and plotted on a logarithmic scale, as shown in Figure 3a. Note that the I_{SC} increases gradually with increasing laser power density ($P_{in} \leq 55$ μW cm^{-2}) in Figure 3b, and the corresponding power factor (α_1) is 0.83. When 55 μW $cm^{-2} < P_{in} \leq 19$ mW cm^{-2}, the power factor (α_2) is 0.39. It means that the probability of photogenerated charges being trapped or recombined gradually increases as the laser power density increases. Moreover, the $|V_{OC}|$ increases first and then decreases with increasing the laser power density. The phenomenon has been confirmed by other laser wavelengths (Figure S15). It suggests that the photogenerated charges can influence the built-in electric field in the asymmetric suspended structure. Note that the surface potential difference between the high and low sides in the asymmetric suspended structure does not originate from the work functions of the Au electrodes or Au/WSe_2 junctions (Figures S16–S17). To further eliminate the influence of factors such as the Schottky barrier, graphene was introduced between the Au electrode and the WSe_2 nanosheet to improve the interface contact, as shown in Figure S18. The results show that the asymmetric suspended Gr/WSe_2/Gr photodetector has the same open-circuit voltage (V_{OC} = -0.1 V) as the asymmetric suspended WSe_2 photodetector. It indicates that the built-in

electric field in the asymmetric suspended WSe_2 photodetector mainly originates from the flexoelectric effect caused by non-uniform strain, and is unrelated to the Schottky barrier between the Au electrode and the WSe_2 nanosheet. Figure S19 shows that the V_{OC} and I_{SC} of the asymmetric suspended WSe_2 photodetector are insensitive to the gate voltage. It indicates that the dominant mechanism in the asymmetric suspended WSe_2 photodetector is the fixed built-in field resulting from flexoelectricity, rather than being dominated by the trap states or carrier concentration that can be tuned by the gate voltage.

The peak position mapping of the first-order Raman-active mode (E^1_{2g}) for WSe_2 in Figure S20 shows that the E^1_{2g} mode in the suspended region has a shift toward lower wave numbers compared to that in the flat region. In addition, the position distribution of E^1_{2g} and B^1_{2g} modes at equidistant spatial positions is asymmetric. It indicates that the asymmetric suspended structure causes different degrees of strain in the WSe_2 nanosheets. Although the low (L) side has a greater strain gradient at a position, the integral transverse field on the L side is smaller than that on the high (H) side due to its smaller channel length (Figure S21). The flexoelectric polarization intensity on the H side of the asymmetric suspended structure is twice than that on the L side after superposition, as shown in Figure S21. For the asymmetric suspended WSe_2 photodetector, the transverse polarization electric field is directed from the H side to the L side. In accordance with the transverse flexoelectric polarization field model, the polarization can be treated as a function of the height profile slope, as shown in Figure S21. The transverse flexoelectric polarization can be expressed as:

$$P_x = \pm\mu \int k/\left(1+k^2\right)dk \tag{1}$$

where P_x is the transverse flexoelectric polarization, μ is flexoelectric coefficient, and k is the slope in the height profile diagram. By integrating according to the analytical model for the transverse polarization field, the built-in electric field is calculated to be ~ 131 mV. This value is comparable to the KPFM measurement (~120 mV, Figure 3c), which directly demonstrates the validity of the analytical model for the transverse polarization field. It greatly simplifies the quantitative study of the transverse component of flexoelectric effect. Strain is calculated based on the relationship between bending strain and the radius of curvature: $\varepsilon = z \times K$, where z is the vertical distance to the neutral axis and K is curvature. The strain on the upper and lower surfaces at the bottom of the channel of the asymmetric suspended WSe_2 nanosheet is ±0.22%, respectively. Figure S22 shows that the transverse strain gradient of the asymmetric suspended WSe_2 can be adjusted by the height difference of the two electrodes, channel width, and nanosheet thickness. Furthermore, the photodetector performance is positively correlated with the transverse strain gradient, as shown in Figure S23. It means that the transverse flexoelectric polarization field plays a dominant role in the self-powered photodetector performance.

Under the same laser power conditions, the $|V_{OC}|$ of the asymmetric suspended WSe_2 photodetector exhibits a first increasing and then decreasing trend with increasing WSe_2 nanosheet thickness, as shown in Figure S24. It indicates that the $|V_{OC}|$ variation trend is consistent with that of the transverse strain gradient modulated by WSe_2 nanosheet thickness (Figure S22d). The $|V_{OC}|$ and I_{SC} of the device show a trend of increasing first and then decreasing with the height difference of the electrodes, as shown in Figure S25. It further proves the high correlation between the height difference of the electrodes and the strain of WSe_2 nanosheets. Meanwhile, the $|V_{OC}|$ and I_{SC} of the asymmetric suspended WSe_2 photodetector linearly vary with the strain of the flexible substrate in the same device (Figure S26). It indicates that the built-in electric field in WSe_2 nanosheets is highly correlated with their degree of strain.

In order to study the coupling mechanism between flexoelectric polarization and optical fields in asymmetric suspended structures, surface potential changes of asymmetric suspended WSe_2 nanosheets under various illumination conditions were investigated by in situ kelvin probe force microscope (KPFM) (Figure S27). The contact potential difference (CPD) between the tip and sample is measured by applying voltage to the tip. The V_{CPD} near the drain (H side) is always higher than that near the source (L side) under dark condition. The illumination increases the V_{CPD} in the source-drain electrode region and channel region near the source. And the V_{CPD} of WSe_2 decreases when the illumination is removed (Figure S27a). Under weak illumination (P_{in} = 2 μW cm^{-2}), the V_{CPD} of the drain region increases more significantly (Figure S27b). The V_{CPD} of the WSe_2 region adjacent to the source electrode rises rapidly until it nearly equals that of the drain electrode as the laser intensity increases. The asymmetric suspended WSe_2 nanosheet forms a surface potential difference (ΔV_{dark} = 120 mV) from drain to source under dark, as shown in Figure 3c. And the ΔV is defined as $\Delta V = V_2 - V_1$, where V_2 and V_1 are the surface potential of the drain and source regions of the WSe_2 nanosheet. When P_{in} = 2 μW cm^{-2}, the surface potential difference across the suspended WSe_2 channel in the source-drain electrode region increases ($\Delta V' > \Delta V_{dark}$). When 0.1 mW $cm^{-2} \le P_{in} \le$ 3.5 mW cm^{-2}, the surface potential difference decreases gradually as the laser power density increases. The change trend is consistent with that of the $|V_{OC}|$ of an asymmetric suspended WSe_2 photodetector under macroscopic conditions. The surface potential difference recovers to the initial level when the laser is switched off.

The linear variation between flexoelectric polarization and strain gradient indicates that non-uniform strain is the main factor contributing to the self-powered capability of the asymmetric suspended WSe_2 device (Figure S28). The variation trends of the effective resistance and V_{OC} of the asymmetric suspended WSe_2 photodetectors under different laser powers are highly consistent with the built-in electric field obtained by KPFM measurement (Figure S29). It indicates that the self-powered capability of the asymmetric suspended WSe_2 photodetector mainly stems from the transverse polarization electric field generated by the flexoelectric effect. In the symmetrical suspended structure, the surface potential difference between the non-suspended and suspended channel regions decreases gradually with increasing laser power density (Figure S30). Note that the surface potential difference of WSe_2 nanosheet has a symmetrical distribution in symmetrical suspended structure, which means that the self-powered capability of the asymmetric suspended WSe_2-based photodetector originates from the asymmetric structure. It indicates that the asymmetric suspended structure enables

effective modulation of the transverse flexoelectric polarization field. Therefore, the asymmetric suspended structure is the main cause of the potential difference at both ends of the WSe_2 nanosheet, and the flexoelectric polarization field can be affected by photogenerated carriers.

Based on the above analysis, the mechanisms of asymmetric structure governed transverse flexo-photoelectric coupling is illustrated in Figure 3d. Under mechanical strain, the separation of positive and negative charges in WSe_2 generates a flexoelectric polarization field, as shown in Figure 3di. KPFM measurements reveal a gradual decrease in surface potential with increasing strain. It indicates that more negative charges accumulate on the surface of WSe_2 nanosheets under the action of mechanical strain. Consequently, a flexoelectric field pointing from the bottom to the top surface forms in the asymmetric suspended WSe_2 structure. Notably, the strain gradients differ on both sides of the channel's lowest point due to the asymmetric structure. The non-uniform continuous deformation of the WSe_2 layer in the asymmetric suspended area causes the non-uniform continuous bending of the energy band. The asymmetry strain generates a non-zero, directionally fixed transverse net field in dark conditions for the asymmetric suspended WSe_2 nanosheet ($E_{in-x} \neq 0$). According to the work function formula: $V_{CPD} = (\phi_{tip} - \phi_{sample})/e$ [11], the low-side region (L) exhibits a higher work function than the high-side region (H) under these conditions ($\Delta\varphi = \phi_D - \phi_S$, $\Delta\varphi < 0$), where ϕ_{tip} is the work function of the tip, ϕ_{sample} is the work function of the sample, and e is the elementary charge. It demonstrates the formation of a persistent built-in electric field oriented from high to low side in the asymmetric suspended WSe_2. Note that the work functions in both H and L sides are lower than that at the channel's lowest point. Under the transverse flexoelectric polarization field, the energy band diagrams on both sides gradually tilt toward the middle region, which provides a prerequisite for the directional flow of photogenerated charges. [57] The asymmetric strain induces two built-in fields of constant magnitude but opposite orientations flanking the channel center, forming a back-to-back electric field configuration. Such opposing fields consistently counteract the carrier drift induced by external driving fields, ultimately yielding the ultra-low dark current in the asymmetric suspended structure.

Under weak illumination ($P_{in} = 2\ \mu W\ cm^{-2}$), the WSe_2 nanosheet rapidly generates a limited population of photogenerated holes and electrons. Notably, the photogenerated carriers in the WSe_2 nanosheet have not yet reached saturation under these conditions. The photogenerated holes and electrons rapidly separate and migrate toward opposite surfaces (upper and lower, respectively) driven by the flexoelectric polarization field, as shown in Figure 3dii. The increased hole concentration elevates the overall surface potential of WSe_2 (Figure S27). The high-side region possesses a larger light-absorbing area due to the structural asymmetry, enabling more photogenerated carriers under the identical laser power density. Consequently, the high-side region exhibits greater surface potential modulation compared to the low-side, amplifying the potential difference across the channel ($|\Delta\varphi_1| > |\Delta\varphi|$). Macroscopically, the $|V_{OC}|$ increases as laser power density increases under weak illumination. The asymmetric suspended WSe_2 photodetector generates a photocurrent flowing from drain to source due to the flexoelectric polarization

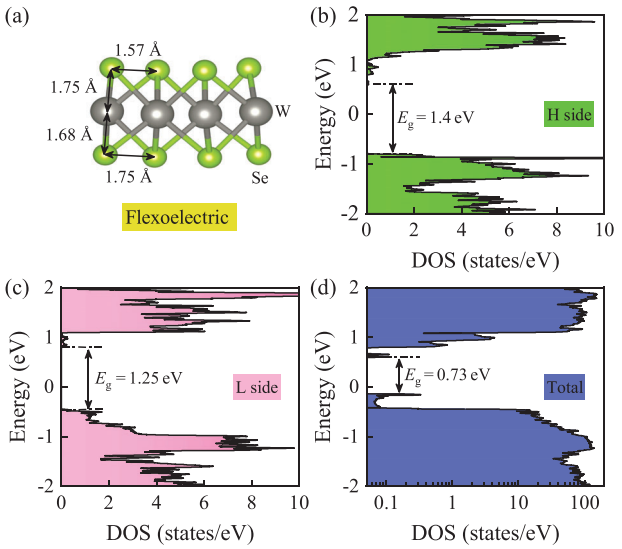

FIGURE 4 | DFT calculations of asymmetric suspended WSe_2 nanosheets. (a) The crystal structure in the flexoelectric state of WSe_2. The density of states (DOS) of WSe_2 nanosheets on the (b) H side and (c) L side. (d) The total DOS of asymmetric suspended WSe_2 nanosheets.

field driving the hole transport from high-side to low-side across the channel under weak illumination.

When $P_{in} \geq 55\ \mu W\ cm^{-2}$, the WSe_2 nanosheet exhibits enhanced photocharge generation. Compared to the low-side region, the high-side region possesses both a larger light-absorption area and a greater potential difference relative to the channel bottom. Consequently, the high-side region reaches saturation rapidly when abundant photocharges are generated. The growing photocharge population in the low-side region progressively reduces the surface potential difference between both sides with increasing laser power density, driving the system toward potential equilibration ($|\Delta\varphi_2| < |\Delta\varphi|$). This reduction in surface potential difference indicates weakened charge-separation capability, which correlates consistently with the observed decrease in power factor (0.83→0.39). The surface potential difference between the high-side and low-side regions progressively decreases with increasing laser power density during this process, leading to a gradual reduction in the conduction band offset between the two WSe_2 nanosheets, as shown in Figure 1diii. Macroscopically, this manifests as a decrease in $|V_{OC}|$ with higher laser power density. Note that the photogenerated carrier density increases with laser power density. Therefore, the I_{SC} increases monotonically during the process. The WSe_2 nanosheet develops two asymmetric back-to-back flexoelectric polarization fields due to the asymmetric suspended structure. And the vector superposition generates an intrinsic built-in electric field (E_{in}), endowing the system with exceptional self-powered photodetection capabilities.

To further investigate the formation mechanism of the built-in electric field in the asymmetric suspended structure, the density of states (DOS) for the asymmetric suspended structure model were calculated using the Atomistix ToolKit (ATK) software package based on density functional theory (DFT). In Figure 4a, the distances between Se atoms on the upper and lower surfaces are 1.57 and 1.75 Å, respectively. It means that the upper and lower surfaces of WSe_2 experienced compressive and tensile strain,

respectively. Compared to the flat model (Figure S31), the W atoms in the asymmetric suspended structure are closer to the lower surface (1.75Å > 1.68 Å). This downward displacement induces a flexoelectric polarization field in WSe_2 along the radial direction [34, 40, 58], with the polarization direction reversing from the concave to the convex surface-consistent with KPFM measurements. The DOS data further confirm that single-layer flat WSe_2 is a semiconductor with a bandgap of 1.54 eV, and this value deviates by less than 5% from the reported experimental value (1.49 eV). It verifies the accuracy of the computational method (Figure S21). The bandgap of WSe_2 decreases nonuniformly across different regions due to biaxial strain, as shown in Figures 4b,c. Compared with the H side, the L side exhibits more obvious edge movement due to its greater strain gradient (Figure S16). The DOS indicates that the introduction of bending strain decreases the bandgap of WSe_2 nanosheet. This provides a prerequisite for expanding the response of WSe_2 films in the infrared region. Particularly, the total DOS suggests that the bandgap of WSe_2 films decreases from 1.54 to 0.73 eV (cf. Figure 4d) under the strain, which is confirmed by the PL spectra (Figure S5). The variation of the bandgap is attributed to the flexoelectric polarization generated by the non-uniform strain. The generation of flexoelectric polarization further leads to the separation of space charges, forming an internal electric field throughout the thickness of the WSe_2 nanosheet [59]. The internal electric field and the lattice distortion caused by the non-uniform strain directly or indirectly change the relative energy between the valence band maximum and the conduction band minimum, ultimately achieving bandgap tuning [16]. It indicates that the flexoelectric effect introduced by mechanical strain can effectively reduce the bandgap of 2D vdW semiconductors, broadening the photoresponse range of 2D materials to infrared region.

2.4 | Optical Communication Technology Based on Asymmetric Suspended Photodetectors

Optical communication is a technology that utilizes light for information transmission, integrating both lighting and communication functions. The light-based data transmission model has the advantages of simplicity, greenness and safety in implementation, and high-speed and low-cost reliable links [2, 60]. At present, optical communication technology has shown a wide range of application scenarios in electromagnetically sensitive places such as hospitals, aircraft cabins, and intelligent transportation. However, optical communication technology still has the disadvantages of high power consumption and low sensitivity in weak illumination detection. The high sensitivity detection of weak illumination signals can be realized without external driving voltage based on the asymmetric suspended structure. In Figure 5a, the infrastructure of the optical communication system mainly includes transmitter, transmission channel and receiver. The light signal to be transmitted in the optical communication system is converted into a digital signal by a signal encoder. With the assistance of a signal generator, the current signal representing a digital signal is sent to transmitter, enabling the conversion of the electrical signal to an light signal. Subsequently, the light signal containing specific information is transmitted through the transmission channel to the light signal receiver, achieving the conversion of the light signal back to a current signal. Finally, the decoder decodes the current signal and retrieves the information, completing the information transmission process. In Figure 5b, the encoder uses the letters representing "ECNU" information for encoding in ASCII as the signal to be transmitted and inputs it into the light signal transmitter. The laser signal with P_{in} = 1.5 μW cm^{-2} is used for data transmission. The signal received by the light receiver based on the asymmetric suspended structure. A good square wave signal and a high matching degree with the input signal represent high-quality transmission of light signals. The light signal receiver based on the asymmetric suspended structure has a responsivity of up to 10^3 A W^{-1}, which indicates that the asymmetric suspended WSe_2-based photodetector can achieve high-quality reception of light signals in an ultra-weak light environment. Finally, the decoder decodes the received current signal and reads the information, thus completing the entire process of information transmission.

Figure 5c and Figure S32 show that the asymmetric suspended WSe_2-based photodetector can generate a stable current signal and achieve a clear signal resolution at P_{in} for more than 1000 s without external bias voltage. In the anti-fatigue characteristic test, 50 pulse signals were continuously applied under the same laser condition for a cyclic testing, as shown in Figure S22a. The pulsed photoresponse signals from the 1st, 5th, 7th, and 9th cycles are extracted. It suggests that the asymmetric suspended WSe_2-based photodetector has excellent signal resolution and stability. Under the condition of a multi-pulse cycle, the change value of the photocurrent is less than 1.75% (Figure S22b). Under continuous constant illumination (P_{in} = 1.5 μW cm^{-2}, V_{DS} = 0 V), the photocurrent signal of the device in the 2500 s time range is stable, and the fluctuation of the current signal is maintained at about 1.4%, as shown in Figure S22c. In Figure 5d, the photodetector utilizing an asymmetric suspended WSe_2 exhibits stable photoelectric performance for over 90 days with current variation remaining below 3.29%. Moreover, the asymmetric suspended WSe_2 nanosheet undergoes a small deformation (~4 nm) for 60 days, which indicates that the photodetectors have a high interface contact stability (Figure S33). The consistent photocurrent output suggests excellent operational stability. It means that asymmetric suspended structure based photodetectors hold significant potential for information transmission. The mechanical cyclic strain results show that after more than 3000 mechanical cyclic strains, the photocurrent and dark current of the asymmetric suspended WSe_2 photodetector are 80% and 3.6 times of the initial values, respectively (Figure S34). It indicates that the device has excellent resistance to mechanical bending interference and fatigue characteristics. The stability results of the photocurrent under different oscillation directions, frequencies, and durations indicate that the WSe_2 photodetector based on the asymmetric suspended structure exhibits excellent oscillation resistance and can maintain stable performance even after experiencing random vibrations (Figure S35).

2.5 | Image Processing Based on Asymmetric Suspended Photodetectors Under Weak Light Conditions

Weak light detection and imaging play a crucial role in various fields such as astronomy, military applications, and medicine.

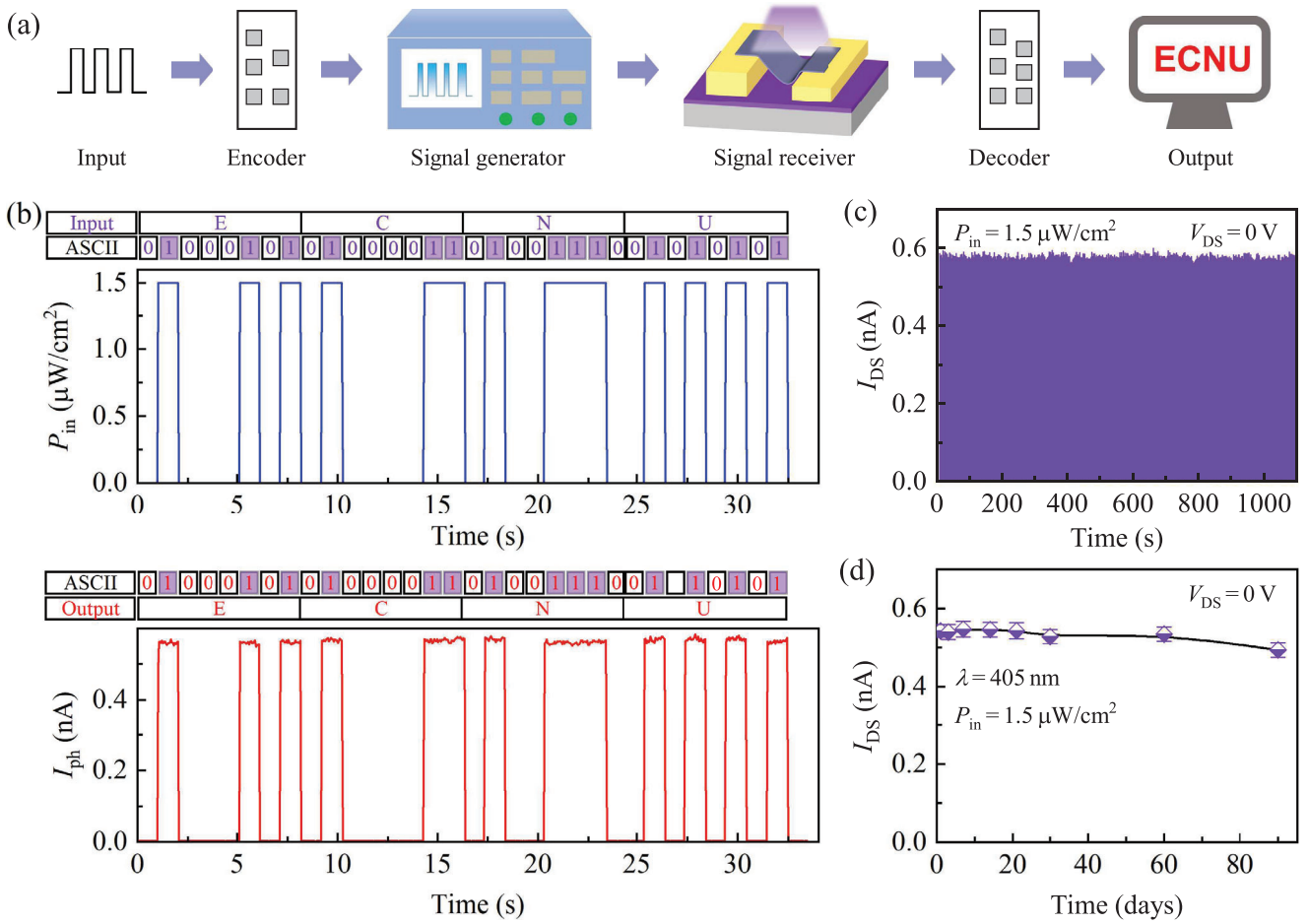

FIGURE 5 | An optical communication system with the asymmetric suspended device. (a) The composition of an optical communication system. (b) The process of realizing accurate information transmission based on an asymmetric suspended structure under ultra-weak light conditions. (c) Photocurrent of an asymmetric suspended WSe_2-based photodetector under continuous laser pulses. (d) The stability of photocurrent for three months (P_{in} = 1.5 μW cm^{-2}, and V_{DS} = 0 V).

[61] The ultra-low dark current and high sensitivity of photodetection enable the device to accurately identify targets in weak light environments. Compared with the conventional field-effect transistor mode (conventional phototransistor), the photodetector based on the asymmetric suspended structure has an ultra-weak light detection capability (*P*min = 1.5 μW cm^{-2}), which is about two orders of magnitude smaller than that of the conventional phototransistor, as shown in Figure 6a. Note that the photocurrent of the WSe_2 photodetector based on the asymmetric suspended structure is 30 times higher than that of the conventional phototransistor under the same laser power density (P_{in} = 18.94 mW cm^{-2}). Figure 6b shows that the on-off ratio of the asymmetric suspended WSe_2 photodetector has been enhanced by four orders of magnitude compared to the conventional WSe_2 photodetector. The excellent ultra-weak light detection capability and high on-off ratio provide the prerequisite for high-precision image recognition.

In Figure 6c, the currents of WSe_2 photodetectors based on asymmetric suspended structure and flat structure under different laser power densities were normalized, respectively. Among them, regions I, II, III, IV, V, and VI correspond to 1.5 μWcm^{-2}, 3.6 μWcm^{-2}, 26 μW cm^{-2}, 0.57 mWcm^{-2}, 3.05 mWcm^{-2}, and 18.94 mW cm^{-2}. After taking the logarithm of the original current data of the asymmetric suspended WSe_2 photodetector, it was mapped to the [0,1] interval through minimum-maximum normalization, which conforms to the actual variation pattern of current levels with light intensity. And the yellow and red boxes respectively represent the noise levels of the flat and the asymmetric suspended structure after normalization, with normalized values of 0.43 and 0. When P_{in} = 1.5 μW cm^{-2}, the normalized values of the WSe_2 photodetectors based on the flat structure and the asymmetric suspended structure are 0.43 and 0.65, respectively. It indicates that the WSe_2 based on the asymmetric suspended structure can effectively identify weak light signals and show obvious image contrast, while the WSe_2 photodetector based on the flat structure cannot determine whether there is light signal input. When P_{in} = 18.94 mW cm^{-2}, the normalized values of the WSe_2 photodetectors based on the flat and the asymmetric suspended structure are 0.78 and 1, respectively. It indicates that the WSe_2 photodetector based on the asymmetric suspended structure has a clearer contrast in image recognition effect. Based on the excellent performance of the asymmetric suspended WSe_2 photodetector, the image recognition process was simulated in the visible light range, as shown in Figure 6d. Compared with conventional photodetectors, the asymmetric suspended WSe_2 photodetector can effectively enhance the contrast of images in dim light and reduce the interference of background noise

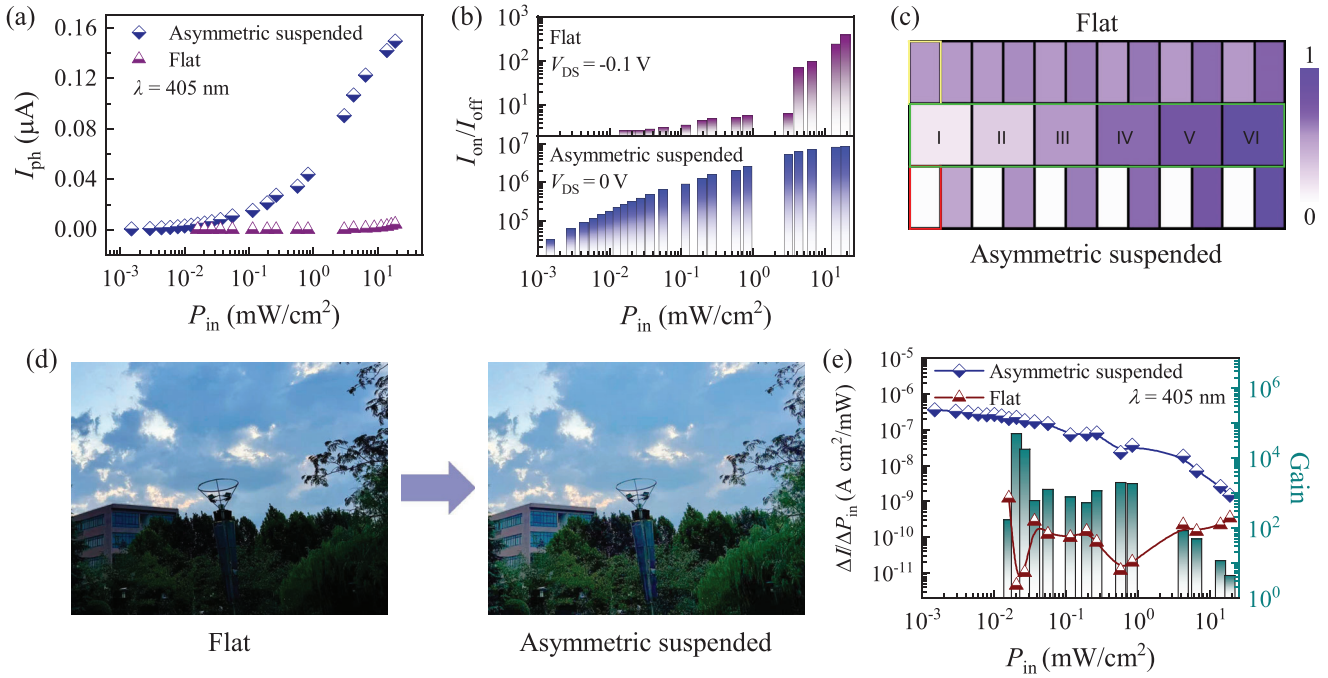

FIGURE 6 | Image recognition enhancement system based on asymmetric suspended structure devices. (a) The photocurrent and (b) Ion/I_{off} of WSe_2 photodetectors based on asymmetric suspended and flat structure under different laser power densities (λ = 405 nm). (c) The comparison diagram of photocurrent of WSe_2 photodetectors based on asymmetric suspended and flat structure under different laser power densities. (d) Image recognition enhancement simulation based on asymmetric suspended WSe_2 photodetector. (e) The recognition ability of WSe_2 photodetectors based on asymmetric suspended and flat structure within the same laser power density range, as well as the gain of the asymmetric suspended structure on WSe_2 photodetectors.

(Note S1). Here, the ratio is used to quantitatively analyze the signal gain of the asymmetric suspended WSe_2 photodetector relative to conventional photodetectors, and the formula is as follows: $G = N_2/N_1$, where N_1 and N_2 represent the photocurrent variation per unit laser power density for the conventional photodetector and the asymmetric suspended WSe_2 photodetector, respectively. This ratio represents the image contrast enhancement between the two photodetectors under identical illumination. The visual gain of the asymmetric suspended WSe_2 photodetector in the image recognition process can be increased by more than two orders of magnitude under the same laser conditions, and even up to more than four orders of magnitude under certain lighting conditions, as shown in Figure 6e. It indicates that the asymmetric suspended WSe_2 photodetector can effectively reduce the interference of background noise and thereby effectively enhance the contrast in the image recognition process.

3 | Conclusion

In conclusion, we propose a novel method for regulating the transverse flexoelectric polarization field by using the asymmetric suspended structure. The coupling effect between the transverse flexoelectric polarization field and the light field enables 2D nanosheets to exhibit excellent self-powered capacity. Taking WSe_2 nanosheets as an example, the asymmetric suspended structure enables them to exhibit outstanding photoelectric performance ($R \sim 6 \times 10^3$ A W^{-1}) and excellent device stability. It indicates that the transverse flexoelectric polarization field formed in the asymmetric suspended structure can effectively suppress the dark current while enhancing the photoresponse. Further develop the transverse flexoelectric polarization field analysis model, and establish a quantitative relationship between the transverse flexural polarization field and the slope of height profile ($P_x = \pm\mu \int k/\left(1+k^2\right) dk$). Combined with first-principles calculations and surface potential measurements, the coupling mechanism of flexoelectric and photoelectronic effects in the asymmetric suspended structure is analyzed from a microscopic perspective. Moreover, the stable ultra-weak light detection capability under 1.5 μW cm^{-2} irradiation demonstrates the potential of the asymmetric suspended structure for information transmission. And the WSe_2-based photodetector by the asymmetric suspended structure can achieve image recognition under weak light. Compared with conventional photodetectors, the visual gain is increased by more than two orders of magnitude. Our work enables superior ultra-weak light detection performance, providing new insights into the development of high-performance self-powered photodetectors and the multidimensional regulation of flexoelectric effects.

4 | Experimental Section

4.1 | Device Fabrication

The fabrication of the asymmetric suspended structure is illustrated in Figure S1. First, a polymethyl methacrylate (PMMA-950K) resist was spin-coated on a clean SiO_2/Si substrate.

After electron beam lithography (EBL) exposure, the designed height Au with a 3 nm-thick Ni adhesion layer was deposited by thermal evaporation. Then, the substrate undergoes a second lithography with various channel distances from 1.5 to 6 μm. Subsequently, 200-nm-thick Au was thermally evaporated in the second etching area to form electrodes with a height difference. WSe_2, InSe, and other 2D layered nanosheets were obtained from the corresponding bulk crystals (Shanghai Onway Techology Co., Ltd) through mechanical exfoliation. Finally, the mechanically exfoliated few-layer WSe_2 nanosheet was transferred to the asymmetric structure substrate by the dry transfer method.

4.2 | Device Characterizations

The morphology and thickness of WSe_2, InSe, and other 2D layered nanosheets were characterized by optical microscopy and atomic force microscopy (AFM Dimension Icon, Bruker), respectively. Raman and photoluminescence (PL) spectra were obtained by a confocal micro-Raman spectrometer (Jobin-Yvon LabRAM HR Evolution, Horiba) with the 532 nm-laser. The surface potentials of WSe_2 was measured by kelvin probe force microscopy system (KPFM Dimension Icon, Bruker).

Asymmetric suspended WSe_2-based photodetector were measured electrically and optically using a Keithley 4200-SCS semiconductor parameter analyzer. All tests were conducted in a vacuum (10^{-6} Torr) and dark environment, and only exposed to the target light source environment. In the photoelectric measurement process, commercial light emitting diodes with laser wavelengths of 405, 520, 638, and 1550 nm were used (Thorlabs, Inc.). The laser spot area was 5 cm^2. A laser diode controller (ITC4001, Thorlabs, Inc.) was used to control the laser to produce light pulses with tunable laser power, laser pulse width, and frequency.

4.3 | First-Principles Calculations

In solving the Kohn-Sham equations, the exchange-correlation potential was described by the generalized gradient approximation (GGA) using the Perdew-Burke-Ernzerhof (PBE) functional. The interaction between nuclei and valence electrons was treated with the SG15 pseudopotential. The valence electron wavefunction was expanded in a linear combination of atomic orbitals (LCAO) basis set. The cutoff energy for the real-space density grid was set to 120 Hartree. Under periodic boundary conditions, the *x*- and *y*-axes were set as the periodic directions of the structure, while the *z*-axis was defined as the non-periodic direction. To eliminate "image" interactions in the non-periodic direction, a vacuum layer exceeding 50 Å was introduced along *z*-axes. During structural optimization, the *k*-point grid in the first Brillouin zone was set to 11×11×1, while electronic property calculations employ a denser 21×21×1 *k*-point grid. All calculations were performed on an optimized geometry where the forces on each atom were converged to below 0.02 eV $Å^{-1}$ and the total energy of the system is converged within 10^{-4} eV $atom^{-1}$. For consistency in analysis and comparison, the Fermi level of all calculated results was aligned to zero.

Author Contributions

Z.T.G., C.Z., and Z.A.H. performed the preparation of 2D layered materials and the construction of heterojunctions, Z.T.G., R.Q.J., and Z.C.H. conducted the experiments for device fabrication and electrical measurements, Z.T.G., and H.L.C. performed the theoretical calculations and data analysis, Z.T.G., H.L.C., L.Y.S., L.Q.Z., Y.W.L., and J.Z. performed the detailed analyses of the underlying mechanism, Z.T.G., J.Z.Z., and Z.G.H. designed the experiments and wrote the manuscript. J.Z. and Z.G.H. supervized the research. All authors have given approval to the final version of the manuscript.

Acknowledgements

This work was financially supported by the National Natural Science Foundation of China (Grant Nos. 62090013 and 62375086), Projects of Science and Technology Commission of Shanghai Municipality (Grant No. 21JC1402100) and the Program for Professor of Special Appointment (Eastern Scholar) at Shanghai Institutions of Higher Learning.

Conflicts of Interest

The authors declare no conflicts of interest.

Data Availability Statement

The data that support the findings of this study are available in the supplementary material of this article.

References

1. X. Duan, Z. Cao, K. Gao, et al., "Bioinspired Toughening of Lightweight Cellular Materials via Multiscale Structural Design," *Advanced Materials* 36 (2024): 2310704.

2. Y. L. Sun, X. G. Zhang, T. J. Cui, and W. X. Jiang, "Programmable Metamaterials for Dynamic Wave Manipulation," *Advanced Functional Materials* 35 (2025): 2421870.

3. K. Feng, Y. Li, Y. Chen, Z. Wei, and G. Shen, "Flexible and Stretchable Electronic Materials for Next-Generation Wearable Devices," *Matter* 8 (2025): 101998.

4. Z. Zhang, T. Cai, Z. Li, et al., "Hierarchical Nanostructures for High-Performance Energy Storage Applications," *Advanced Materials* 37 (2025): 2413771.

5. Y. Han, S. Jiao, X. Zhang, et al., "Advanced Functional Nanomaterials for Energy Conversion and Storage," *Advanced Materials* 37 (2024): 2416935.

6. M. Gedda, H. Song, A. R. Pininti, et al., "Recent Advances in Mechanical Metamaterials: Design, Fabrication, and Applications," *Materials Science and Engineering: R: Reports* 162 (2025): 100885.

7. L. Chen, T. Lin, J. Chai, et al., "Enhanced Microwave Absorption in Engineered Metamaterial Structures," *Applied Physics Letters* 126 (2025): 122107.

8. Q. Jiang, K. Wang, F. Wang, et al., "Ultrathin Two-Dimensional Nanomaterials for High-Performance Nanoelectronics," *ACS Nano* 18 (2024): 25249–25256.

9. B. Kim, S. Y. Lee, H. Ko, et al., "Stretchable and Wearable Electronics Based on Nanomaterial Systems," *Nature Nanotechnology* 20 (2025): 237–245.

10. Y. Jiang, C. Liao, X. Qin, et al., "Smart Responsive Materials for Adaptive Electronics and Sensing Systems," *Advanced Functional Materials* 35 (2025): 2422304.

11. Z. Gao, R. Jiang, M. Deng, et al., "Advanced Functional Architectures for High-Performance Flexible Electronic Materials," *Advanced Materials* 36 (2024): 2401585.

12. Q. Gao, H. Meng, E. Wu, X. Zhuang, and Y. Li, "Design Strategies for High-Performance Functional Polymer Materials," *Advanced Functional Materials* 35 (2025): e20981.

13. L. Lv, F. Zhuge, F. Xie, et al., "Self-Powered Electronic Systems Based on Nanostructured Functional Materials," *Nature Communications* 10 (2019): 3331.

14. R. Kumar, A. K. Shringi, H. J. Wood, et al., "Recent Progress in Advanced Engineering Materials for Structural and Functional Applications," *Materials Science and Engineering: R: Reports* 163 (2025): 100946.

15. G. Wang, Y. Sun, Z. Yang, et al., "Flexible and Stretchable Electronic Devices Based on Advanced Functional Materials," *Advanced Functional Materials* 34 (2024): 2316267.

16. H. Zeng, H. Yu, B. Liu, et al., "High-Performance Smart Materials for Adaptive and Responsive Systems," *Advanced Functional Materials* 34 (2024): 2400712.

17. Y. Mu, J. Yang, G. Xie, Z. Wang, B. Guo, and J. R. Gong, "Bioinspired Tough and Stretchable Materials for Next-Generation Flexible Devices," *Advanced Functional Materials* 34 (2024): 2315543.

18. B. Li, L. Zheng, Y. Gong, and P. Kang, "Emerging Materials for Sustainable Energy Storage and Conversion," *Materials Today* 81 (2024): 118–136.

19. X. Du, W. Tian, J. Pan, et al., "Nanostructured Materials for High-Efficiency Energy Storage Applications," *Nano Energy* 92 (2022): 106694.

20. S. Aftab and H. H. Hegazy, "Recent Advances in Miniaturized Functional Materials and Devices," *Small* 19 (2023): 2205778.

21. W. Wu, L. Wang, Y. Li, et al., "Piezoelectricity of Single-Atomic-Layer MoS_2 for Energy Conversion and Piezotronics," *Nature* 514 (2014): 470–474.

22. C. Zhang, M. Y. Li, J. Tersoff, et al., "Interlayer Coupling and Band Alignment in MoS_2/WSe_2 van der Waals Heterostructures," *Nature Nanotechnology* 13 (2018): 152–158.

23. G. da Cunha Rodrigues, P. Zelenovskiy, K. Romanyuk, S. Luchkin, Y. Kopelevich, and A. Kholkin, "Strong Piezoelectricity in Single-Layer MoS_2 Deposited on SiO_2," *Nature Communications* 6 (2015): 7572.

24. H. Chen, C. Hu, L. Chen, et al., "Spin Dynamics and Magnetic Phase Transitions in Low-Dimensional Quantum Systems," *Physical Review B* 110 (2024): 014102.

25. X. Wang, X. Zhou, A. Cui, et al., "Recent Advances in Flexible and Stretchable Electronic Materials," *Materials Horizons* 8 (2021): 1985–1997.

26. W. Li and J. Li, "Electric Field Control of Magnetism in Two-Dimensional Materials," *Nature Communications* 7 (2016): 10843.

27. M. I. B. Utama, H. Zeng, T. Sadhukhan, et al., "Twistronics and Emergent Phenomena in van der Waals Heterostructures," *Nature Communications* 14 (2023): 2193.

28. X. Tang, H. Jiang, Z. Lin, X. Wang, W. Wang, and G. Li, "Recent Progress in Nano-Micro Structured Materials for Energy and Sensing Applications," *Nano-Micro Letters* 17 (2024): 56.

29. J. Sun, S. Gao, C. Zhang, L. Xu, J. Tan, and Z. Dai, "Advanced Functional Interfaces for High-Performance Electronic and Energy Devices," *ACS Applied Materials & Interfaces* 17 (2025): 55143–55152.

30. R. Mastria, K. J. Riisnaes, A. Bacon, et al., "Multifunctional Materials for Next-Generation Flexible and Wearable Electronics," *Advanced Functional Materials* 34 (2024): 2401903.

31. X. Yu, Z. Peng, L. Xu, et al., "Flexible and Stretchable Functional Materials for Wearable Electronics," *Small* 20 (2024): 2402561.

32. H. Liu, Q. Lai, J. Fu, S. Zhang, Z. Fu, and H. Zeng, "Tailoring Two-Dimensional Materials for Advanced Electronic and Energy Applications," *Nature Communications* 15 (2024): 4556.

33. P. Guo, M. Jia, D. Guo, Z. L. Wang, and J. Zhai, "Triboelectric Nanogenerators for Self-Powered Systems and Smart Electronics," *Matter* 6 (2023): 537–553.

34. L. Wang, S. Liu, X. Feng, et al., "High-Performance Nanostructured Materials for Flexible and Wearable Devices," *Nature Nanotechnology* 15 (2020): 661–667.

35. W. Ming, B. Huang, S. Zheng, et al., "Emerging Two-Dimensional Materials with Novel Electronic and Mechanical Properties," *Science Advances* 8 (2022): eabq1232.

36. Y. Zou, Z. Zhang, J. Yan, et al., "Advanced Functional Nanomaterials for Energy Conversion and Storage Applications," *Nature Communications* 13 (2022): 4372.

37. M. Deng, X. Wang, X. Xu, et al., "Recent Progress in Materials Horizons for Flexible and Intelligent Systems," *Materials Horizons* 10 (2023): 1309–1323.

38. B. Huang, Y. Yu, F. Zhang, et al., "High-Performance Advanced Materials for Next-Generation Electronics," *Advanced Materials* 35 (2023): 2305766.

39. L. Qi, W. Tang, X. Weng, et al., "Smart Functional Materials for Adaptive and Responsive Devices," *Advanced Functional Materials* 34 (2024): 2315991.

40. J. Narvaez, F. Vasquez-Sancho, and G. Catalan, "Enhanced Flexoelectricity in Ferroelectric Materials at the Nanoscale," *Nature* 538 (2016): 219–221.

41. C. Chen, H. Liu, Q. Lai, et al., "Nanostructured Materials for High-Performance Energy Conversion and Storage," *Nano Letters* 22 (2022): 3275–3282.

42. Y. Pan, L. Zhu, L. Lu, et al., "Advanced Functional Materials for Flexible and Wearable Electronics," *Advanced Functional Materials* 34 (2024): 2407931.

43. Y. Luo, J. Zhao, A. Fieramosca, et al., "Light–Matter Interaction in Engineered Photonic Structures," *Light: Science & Applications* 13 (2024): 203.

44. J. Yu, B. Huang, S. Yang, et al., "Two-Dimensional Nanomaterials for Next-Generation Electronic Devices," *Nano Letters* 24 (2024): 6337–6343.

45. X. Yang, X. Liu, L. Qu, et al., "Carbon-Based Nanomaterials for Energy Storage and Conversion," *ACS Nano* 16 (2022): 8440–8448.

46. J. Peng, G. Zou, J. Huo, et al., "Nanostructured Energy Materials for High-Efficiency Energy Harvesting," *Nano Energy* 117 (2023): 108891.

47. M. Dai, H. Chen, F. Wang, et al., "Advanced Nanostructures for High-Performance Electronic and Energy Devices," *ACS Nano* 14 (2020): 9098–9106.

48. Y. Liao, Y. J. Kim, and M. Kim, "Recent Advances in Chemical Engineering Materials for Energy and Environmental Applications," *Chemical Engineering Journal* 476 (2023): 146838.

49. X. Ren, X. Li, X. He, et al., "Functional Materials for Catalysis and Energy Conversion Applications," *Chemical Engineering Journal* 496 (2024): 153937.

50. Y. Huang, Y. K. Wang, X. Y. Huang, et al., "Emerging Information Materials for Next-Generation Electronics and Photonics," *InfoMat* 4 (2022): e12274.

51. Q. Cheng, J. Pang, D. Sun, et al., "Recent Advances in Flexible and Stretchable Energy Storage Devices," *InfoMat* 2 (2020): 656–697.

52. C. Xie, C. K. Liu, H. L. Loi, and F. Yan, "Perovskite-Based Photodetectors and Their Applications in Optoelectronics," *Advanced Functional Materials* 30 (2020): 1903907.

53. R. Ding, Y. Lyu, Y. Zhao, et al., "Emerging Materials for Energy Conversion and Storage Applications," *Materials Today Physics* 28 (2022): 100867.

54. Y. Pan, T. Zheng, F. Gao, et al., "Flexible Functional Materials for Wearable and Portable Electronics," *Small* 20 (2024): 2311606.

55. X. Cao, Z. Lei, B. Huang, et al., "Smart Nanomaterials for Advanced Sensing and Electronic Devices," *Small* 18 (2022): 2200445.

56. M. Che, B. Wang, X. Zhao, et al., "Advanced Nanostructured Materials for High-Performance Energy Applications," *ACS Nano* 18 (2024): 30884–30895.

57. R. Guo, L. You, W. Lin, et al., "Ferroelectric Domain Engineering for High-Performance Electronic Devices," *Nature Communications* 11 (2020): 2571.

58. X. Wen, D. Li, K. Tan, Q. Deng, and S. Shen, "Fundamental Limits of Energy Conversion in Nanoscale Systems," *Physical Review Letters* 122 (2019): 148001.

59. X. Liang, H. Dong, Y. Wang, et al., "Advanced Functional Materials for Next-Generation Flexible Electronics," *Advanced Functional Materials* 34 (2024): 2409906.

60. L. E. M. Matheus, A. B. Vieira, L. F. M. Vieira, M. A. M. Vieira, and O. Gnawali, "A Survey of Communication Protocols for Internet of Things Applications," *IEEE Communications Surveys & Tutorials* 21 (2019): 3204–3237.

61. K. Dong, H. Zhou, Z. Gao, et al., "Flexible and Stretchable Energy Harvesting Devices Based on Advanced Functional Materials," *Advanced Functional Materials* 34 (2023): 2306941.

Supporting Information

Additional supporting information can be found online in the Supporting Information section.

Supporting File: adfm75226-sup-0001-SuppMat.pdf.